King Saud University

Arabian Journal of Chemistry

www.ksu.edu.sa
www.sciencedirect.com

ORIGINAL ARTICLE

Development of a new vesicular formulation for delivery of Ifosfamide: Evidence from *in vitro*, *in vivo*, and *in silico* experiments

Mohammad Reza Hajinezhad [a], Sheida Shahraki [b], Zahra Nikfarjam [c], Fatemeh Davodabadi [d], Shekoufeh Mirinejad [b], Abbas Rahdar [e], Saman Sargazi [b,f,*], Mahmood Barani [g,**]

[a] *Basic Veterinary Science Department, Veterinary Faculty, University of Zabol, Zabol P. O. Box. 98613-35856, Iran*
[b] *Cellular and Molecular Research Center, Research Institute of Cellular and Molecular Sciences in Infectious Diseases, Zahedan University of Medical Sciences, Zahedan 98167-43463, Iran*
[c] *Department of Physical & Computational Chemistry, Chemistry and Chemical Engineering Research Center of Iran, Tehran, Iran*
[d] *Department of Biology, Faculty of Basic Science, Payame Noor University, Tehran, Iran*
[e] *Department of Physics, University of Zabol, Zabol P. O. Box. 98613-35856, Iran*
[f] *Department of Clinical Biochemistry, School of Medicine, Zahedan University of Medical Sciences, Zahedan, Iran*
[g] *Medical Mycology and Bacteriology Research Center, Kerman University of Medical Sciences, Kerman 7616913555, Iran*

Abstract Ifosfamide (IFO) is a member of the oxazaphosphorine family of alkylating drugs that exhibits anticancer and immunoregulatory properties. The toxicity of IFO is dose-limited because of its biotransformation into highly reactive metabolites, including acrolein and chloroacetaldehyde. Here, we aimed to design novel niosomal formulations to encapsulate IFO within niosomes and assess the efficacy of the nanoformulation via conducting in vivo, in vitro, and in silico analyses. Niosomal IFO showed a monodisperse size distribution with an average size of 97 nm. In addition, transmission electron microscopy (TEM) revealed a spherical morphology with high stability

* Corresponding author at: Cellular and Molecular Research Center, Research Institute of Cellular and Molecular Sciences in Infectious Diseases, Zahedan University of Medical Sciences, Zahedan, Iran.
** Corresponding author at: Medical Mycology and Bacteriology Research Center, Kerman University of Medical Sciences, Kerman 7616913555, Iran.
E-mail addresses: hajinezhad@uoz.ac.ir (M.R. Hajinezhad), sheida.shahraki@gmail.com (S. Shahraki), nikfarjam.zahra14@gmail.com (Z. Nikfarjam), nikfarjam.zahra14@gmail.com (F. Davodabadi), shokufemn@gmail.com (S. Mirinejad), a.rahdar@uoz.ac.ir (A. Rahdar), sgz.biomed@gmail.com, sgz.biomed@zaums.ac.ir (S. Sargazi), mahmoodbarani7@gmail.com (M. Barani).
Peer review under responsibility of King Saud University.

Production and hosting by Elsevier

and no aggregation. On the other hand, niosomal IFO (0.01–100 µg/mL) showed high cytotoxicity against breast cancer (MCF7) and neuroblastoma (SH-SY5Y) cells in a concentration-dependent fashion. IFO-loaded niosomes had lower IC_{50}s in cancerous cell lines than the standard IFO, the most pronounced being in SH-SY5Y cells (IC_{50} = 0.184 µg/mL). Intravenous treatments of rats with niosomal IFO at 0.1 mg/kg body weight (bw) and 0.2 mg/kg bw significantly increased biochemical parameters such as blood urea nitrogen (BUN), creatinine (CR), alanine aminotransferase (ALT), and aspartate aminotransferase (AST). Moreover, the 0.2 mg/kg bw doses of niosomal IFO caused obvious changes in the liver tissue. Both 0.1 mg/kg bw and 0.2 mg/kg bw doses of free IFO caused histopathological lesions and significantly increased biochemical parameters. In silico calculations revealed the interaction of IFO through its oxygen and nitrogen connected to the phosphor atom and nitrogen with a head group of Span 60 and tween 60. For the first time, we designed a well-characterized niosomal formulation for the targeted delivery of IFO. Our formulation exhibited optimum size with desirable anticancer activity and can be considered a suitable carrier with a high potential for future usage in the controlled release of other chemotherapeutics; however, more studies are needed to assess its safety towards normal human cells.

1. Introduction

Cancer is a condition in which the cells divide and grow uncontrollably, and it is a leading cause of mortality worldwide. In 2020, cancer was responsible for almost one in six deaths globally, with a total of nearly 10 million lives lost (Cancer, n.d.; Harati-Sadegh et al., 2021). Surgery, radiotherapy, and chemotherapy are procedures used for cancer management (Luqmani, 2005; Ghaznavi et al., 2021). The pharmacokinetic profiles of chemotherapy drugs and their non-specific distribution among many organs and tissues are poorly controlled, resulting in severe side effects (Danhier et al., 2010; Barani et al., 2021). Cancer cell resistance to almost all chemotherapeutic medicines and targeted drugs is widespread. Around 80 to 90 percent of mortalities in cancer patients are directly or indirectly attributed to drug resistance (Zahreddine and Borden, 2013). The inhibition of tumor growth induced by chemotherapeutic drugs could be stopped due to a lack of response due to cell resistance. It might be a cellular response to drug exposure or inherent in a subpopulation of heterogeneous cancers (Luqmani, 2005). Several mechanisms are involved in the chemotherapy resistance of tumors. For instance, the increase in the expression of membrane transporter, ATP binding cassette (ABC), improves drug efflux. Several of the 48 ABC transporters in humans have been associated with cancer chemoresistance, including P-glycoprotein and Multidrug resistance-associated protein-1 (Zahreddine and Borden, 2013). In addition to interfering with the transport of drugs into tumor cells, they also pump them out of the cancer cells, which contributes to intrinsic drug resistance. Additionally, cancer cells can acquire specific genetic or epigenetic abnormalities over time that contribute significantly to drug resistance (Nikolaou et al., 2018).

Nanotechnology has various potential applications in medicine, from drug delivery to imaging and diagnosis (Laraib et al., 2022). Nanoparticles can be designed to target specific cells or tissues in the body, which can improve the effectiveness of drug delivery while reducing side effects (Safaei et al., 2019). Nanoparticles can also be used in medical imaging, such as magnetic resonance imaging (MRI) and computed tomography (CT) scans, to provide higher-resolution images of the body's internal structures. Additionally, nanotechnology can be used to develop biosensors that can detect disease biomarkers, allowing for earlier and more accurate diagnosis of diseases like cancer (Salarpour et al., 2022; Roostaee et al., 2022; Roostaee and Sheikhshoaie, 2022). Overall, the use of nanotechnology in medicine has the potential to revolutionize the way we prevent, diagnose, and treat diseases (Roostaee et al., 2022). Administration methods by use of nanotechnology have been effective in overcoming drug resistance caused by cancer. In cancer treatment, a mixed approach of targeted therapies and nanotechnology is a promising methodology to overcome drug resistance (Gao et al., 2015). Nanocarriers are a class of drug delivery vehicles that show great promise in the field of medicine. They are composed of a variety of biodegradable materials that are engineered to have a size of < 100 nm (Suri et al., 2007). Liposomes, lipid-based nanoparticles with high potential in enhancing cancer therapy, can incorporate and/or associate with several molecules as cancer drugs. Due to the potential that Liposomes have in the controlled release of anticancer low-molecular-weight medicines, they are considered a popular platform among all (Gu et al., 2020). Many reports have focused on phospholipid vesicles and liposomes, but they have several disadvantages, including chemical instability. In addition to their cost and variable purity, natural phospholipids may have other considerations. From a technical perspective, alternative phospholipids may be interesting (Baillie et al., 1985).

A niosome consists primarily of a nonionic surfactant, additives, and forming a lipid bilayer with an aqueous center. Drugs in the aqueous core are hydrophilic, while those in the lipid bilayer are hydrophobic (Bhardwaj et al., 2020). They offer several advantages over liposomes, including greater chemical stability, enhanced penetration, and lower costs (Nasr et al., 2008). It is possible to deliver drugs sustainedly, controlled, and targeted using niosomes, which contain cholesterol-containing surfactants in the vesicular layer, as well as additives in the niosome preparation (Bhardwaj et al., 2020; Junyaprasert et al., 2008). As an integral component of the cell membrane, it affects fluidity and permeability. Having a steroidal system (cholesterol) enhances the strength of the bilayer. Thus, drug molecules in this system are protected from inactivation and degradation before they become mature because of the unwanted immunological and pharmacological effects (Rajera et al., 2011). Non-ionic surfactants lacking any polar-head charges are commonly utilized to control drug delivery's kinetics, persistence, and location (Moghassemi and Hadjizadeh, 2014).

The application of niosome, a vesicle produced from nonionic surfactants, is being studied as a potential new drug delivery platform. The molecular structure of surfactants is such that they tend to self-organize into a bilayer. Hydrophilic surfactant ends tend to cluster together on the outside of the structure, while hydrophobic ends cluster together on the inside. Due to their lamellar architecture, these carriers can simultaneously entrap two distinct types of pharmaceuticals (Khoee and Yaghoobian, 2017). Tavano et al. prepared pH-sensitive niosomes to deliver drugs to hepatoblastoma cells with conjugated Pluronic doxorubicin (Dox) niosomes. With surface modification, hepatoblastoma cells were targeted without pH-sensitive molecules. Upon penetration, amino groups on the niosomes are protonated, releasing their cargo (Tavano et al., 2013; Masotti, 2013).

First developed by Asta-Werke, Ifosfamide (IFO, 3-(2-chloroethyl)-2-[(2-chloroethyl) amino] tetrahydro-2H-1,3,2-oxazaphosphorine-2-oxide) is an alkylating agent related to oxazaphosphorine. As a result of its biotransformation to form highly reactive metabolites like acrolein and chloroacetaldehyde, IFO exhibits antitumor and immunomodulatory properties but has dose-limiting toxicity. Since chemotherapy drugs cause systemic toxicity in patients, rapid cell division can lead to targeted sites for chemotherapy drugs. On the other hand, high doses of this drug are associated with cardiotoxicity, encephalopathy, urotoxicity, nephrotoxicity, and neurotoxicity (Giraud et al., 2010). IFO is a white crystalline hygroscopic powder with water solubility of about 100 mg/ml and a melting point of 40 °C. It is used to treat several solid tumors such as the endometrium, cervix, ovary, testes, lung, and thymus as well as sarcoma and Burkitt's lymphoma. In acidic media, IFO undergoes hydrolytic degradation at a definite rate depending on the pH of the solution (Alexander et al., 1993). The stability, uptake, and permeability of IFO have been enhanced in several previous studies by incorporating it into different nanocarriers. As a part of the formulation, IFO was integrated into the following formulations: self-micro emulsifying drug delivery systems, solid-lipid nanoparticles, self-assembled polymeric nanoparticles, span 80 nanovesicles, and nanostructured lipid nanoparticles (Velmurugan and Selvamuthukumar, 2016; Chen et al., 2015; Pandit and Dash, 2011; Ujhelyi et al., 2015).

To improve drug delivery while minimizing undesirable side effects, we developed a novel niosomal formulation with Span 60 and Tween 60 as the drug carrier in this study. We hypothesized that IFO encapsulation in the niosome would enhance its therapeutic effect due to nanometric size and enhanced cellular uptake. The dynamic light scattering, morphology, and encapsulation efficiency analyses were carried out to characterize the formulations. The *in vitro* and *in vivo* toxicity of the developed formulation was examined, and finally, the atomic interactions of the IFO molecule and lipid bilayer were modeled by dynamic simulations.

2. Material and method

2.1. Chemicals and cell lines

Phosphate-buffered saline (PBS), antibiotic–antimycotic solution, and trypsin- ethylenediaminetetraacetic acid (EDTA) solution were obtained from INOCLON (Tehran, Iran). Dulbecco's modified eagle medium (DMEM) and fetal bovine serum (FBS) were purchased from Biochrome (Berlin, Germany). IFO, Span 60, Tween 60, cholesterol (Chol), dimethyl sulfoxide (DMSO), and methyl-thiazolyl-tetrazolium (MTT) were purchased from Sigma-Aldrich Chemical Co. (St. Louis, MO, USA). All plastic materials were procured from Sorfa (Zhejiang, China).

Cancerous [human breast cancer (MCF-7) and Human neuroblastoma (SH-SY5Y)] and non-cancerous [human umbilical vein endothelial cells (HUVECs)] cell lines were obtained from the cell repository of the Pasteur Institute of Iran (Tehran, Iran), cultivated in DMEM medium supplemented with antibiotic–antimycotic solution [penicillin (100 units/mL)/streptomycin (100 µg/mL)/amphotericin B (250 µg/mL)] and 10% heat-deactivated FBS. Cells were grown in standard conditions as previously described (Saravani et al., 2020).

2.2. Preparation of niosomal formulation

Niosomal formulations were synthesized using Chol, Tween 60, and Span 60 at molar concentrations of 0.30:0.35:0.35

and a total lipid concentration of 200 µM. Span 60, Tween 60, and Chol were dissolved in chloroform, and a thin dry film was formed after the organic solvent was evaporated using a rotary evaporator (VR 4, Varghatajhiz, Tehran, Iran). The setup parameters of the rotary evaporator were 180 rpm, 60 °C temperature, and vacuum. Thin layer films were hydrated with IFO solution and evaporated at 60 °C for 30 min. To assess encapsulation efficiency (EE%), the prepared niosomal IFO were centrifuged at speed of 15000 rpm for 30 min. A UV–Vis spectrophotometer (Cary 100, Agilent, USA) operating at a wavelength of 230 nm was then used to measure the absorbance of the supernatant.

2.3. Analysis of the particle size and size distribution

Using a Zetasizer Nano-S90 (Malvern Instruments, Malvern, UK) and a 633 nm He-Ne laser beam at a fixed scattering angle of 90°, the average particle size and size distribution analyses were conducted. To measure the particle size, niosomal IFO was diluted in a solution. The tests were carried out in triplicate.

2.4. Transmission electron microscopy

A transmission electron microscope was used to analyze the morphology of the niosomal IFO (TEM, Philips, EM 208S, Eindhoven, Netherlands). The niosome dispersion was diluted several times with ultra-pure water before further examinations. The carbon-coated copper grid was dyed with 2% phosphotungstic acid after applying the aqueous solution. The samples were observed under TEM after being dried using infrared light.

2.5. Simulation studies

2.5.1. Setup and parametrization of the forcefield

It is critical to define specific interactions with niosome substances in order to understand the solubility and loading of IFO in systems containing the medication. To enable the capability of evaluating such interactions with great precision, a basic model is required. The Lipid17 force field, a developed version of the lipid 14 force field for lipids, specified the characteristics of every component of the noisome bilayer (Dickson et al., 2014). The HF/6-3G (d,p) level of theory was used to optimize the structures of tween 60, Span 60, and cholesterol. However, the RESP methodology is used to get the geometrically most reliable structure and obtain the atomic partial charge of each atom (Vanquelef et al., 2011). Using the ACPYPE Python tool, AMBER coordinate, and topology files have been transformed towards GROMACS-acceptable formats (Sousa da Silva and Vranken, 2012).

Employing GAFF forcefield of AmberTools20, force filed parameters for IFO (Case et al., 2018). At the B3LYP/ 6—311 + +G** level of theory, the RESP charge method was employed to extract the atomic charge from the result of the geometrically optimized structure of IFO.

2.5.2. Details of the bilayer setup and simulation

By collecting the PubChem structures, then afterward optimizing geometrically in HF/6-311G (d,p) level of theory, the noi-

some bilayer was first created by cholesterol, Span 60, and between 60 using the CELL microcosmos 2.2 tool (Sommer et al., 2011). For the construction of the bilayer, there were 78, 78, and 156 molecules of each molecule with a 25:25:50 M ratio for cholesterol, tween 60, and Span 60, respectively. Each bilayer component was distributed at probability sampling within a 5.90 nm box, with the hydrophilic heads and hydrophobic portions arranged in opposition to each other.

According to Figs. 1, 10 IFO molecules were introduced into the bilayer's topmost layer to investigate how these molecules can interact with the noisy bilayer. In order to further closely duplicate the water's surface tension, in an SPC/E water box, the generated structure was subsequently solvated (Chen and Smith, 2007). The generated noisy bilayer was subjected to energy minimization and then the steepest descent algorithm was used to prevent unexpected atom overlap. To eliminate any leftover collisions between atoms in the box, a quick simulation annealing process lasting 100 ps was carried out at 500 K. After that, the industry underwent an NVT simulation run for 500 ps at 298 K to acclimate the system's temperature. This temperature was chosen because it creates the best circumstances for creating the most stable niosome vesicles (Nasseri, 2005). In this procedure, the water and IFO were linked independently from the Span 60, tween 60, and cholesterol, which used to have a coupling constant of 0.1 ps and were connected to the v-rescale thermostat. The resulting arrangement was then put through a 5-ns NPT simulation utilizing a semi-isotropic Berendsen barostat (Berendsen et al., 1984) to maintain the system's temperature and pressure at 298 and 1 bar, respectively. All three orientations were subjected to periodic boundary conditions. The LINCS algorithm was used to apply bond constraints, and the Fast Particle Mesh Ewald (PME) approach was employed to calculate electrostatic interactions (Berendsen et al., 1995). Then, 1.5 nm has been selected as the cutoff for the Coulomb and van der Waal interactions. In Gromacs 2020.1 package, the systems were modeled for quite a 100 ns production run.

2.6. In vitro cytotoxicity assessments

We used MTT colorimetric assay to measure cells' metabolic activity following exposure to standard IFO, niosomal IFO, and unloaded niosomes in cancerous cells and HUVECs (Twentyman and Luscombe, 1987). This assay is based on the ability of viable cells to reduce the water-soluble yellow-colored MTT dye to purple-colored formazan crystals that cannot be dissolved in water. For this purpose, cells were incubated with high glucose-DMEM media, seeded in 96-well plates (180 µL of cell suspension containing 5000–6000 cells/well), and maintained in an incubator at 37 °C. The next day, escalating concentrations of the three agents (0.01 to 100 µg/mL) were added to the plates and incubated for 48 h. Then, 20 µL of MTT solution (5 mg/mL in PBS) was added to each well. After 4 h of incubation, the cell's supernatant was replaced with 200 µL of DMSO solution, and the plates were placed on a shaker to enhance the dissolution of formazan crystals. Finally, the color density was measured at 570 nm via a spectrophotometer. Cell viability was determined as previously described (Sargazi et al., 2019) and reported as a percentage. The IC_{50} value was calculated by using a linear regression equation from the viability graph. Morphological alterations in MCF7 breast cancer cells treated with 1–10 µg/mL of standard and niosomal IFO were monitored after 48 h treatment, and images were captured via an inverted optical microscope (OLYMPUS IX71, Olympus, Tokyo, Japan).

2.7. In vivo assessments

2.7.1. Animal handling and experimental procedure

Male Wistar rats (271–302 g; 80 days old) were housed in polycarbonate cages under standard room temperature (20 to
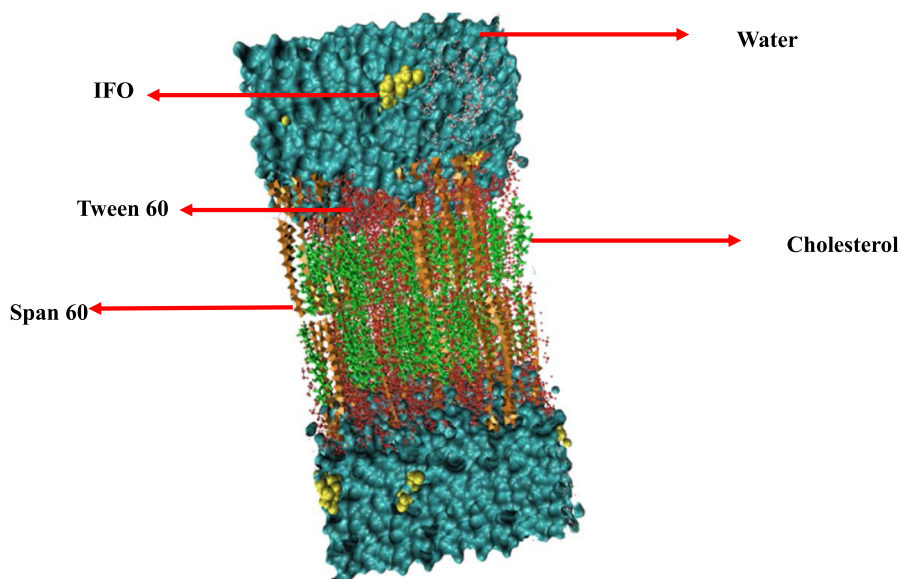

Fig. 1 Schematic of studied compounds after molecular dynamics simulation. The beginning of a noisy bilayer with ten IFO medicines at the top. The molecules of Span 60, Tween 60, and cholesterol are depicted as orange, red, and green, respectively. Water molecules are shown as surfaces along with IFO molecules, like the VDW drawing method.

22 °C) and naturallight–dark circle. Rats were obtained from our breeding colony. Rats were housed in a well-ventilated colony room and given ad-lib access to chow and tap water for the experiments. Animals were randomized into five groups (n = eight rats in each group): (1) control group received an intravenous infusion of normal saline (0.9% sodium chloride in 5% dextrose) and served as a placebo. The other four groups were designed as treatment groups and were treated intravenously with bulk IFO and niosomal IFO at 0.1 mg/kg and 0.2 mg/kg doses three times at 72 h intervals (every 2 weeks for a total of five treatment courses). After completing the injection procedure, blood samples were collected from the *retro*-orbital sinus. For histopathological analysis, rats were subjected to CO_2 euthanasia followed by guillotine amputation. Finally, liver and kidney samples were routinely processed, embedded in 10% neutral buffered formalin, sectioned at a thickness of 5 μm, and stained with hematoxylin-eosin (H&E) and Masson's trichrome staining.

2.7.2. Serum biochemical parameters

Blood samples were centrifuged at 5000 × g for ten min to obtain serum. Collected serum samples were stored at − 20 °C until biochemical analysis. Serum biochemical parameters were determined by the Selectra Pro M auto-analyzer. (Vital Scientific, SpanNeren, Netherlands). Commercial kits from Pars Azmoon biochemical company (Tehran, Iran) were used to determine blood urea nitrogen (BUN), creatinine (CR), alanine aminotransferase (ALT), and aspartate aminotransferase (AST). Hepatic malondialdehyde (MDA) concentrations were measured by the method of Ohkawa et al. (Ohkawa et al., 1979).

2.8. Statistical analysis

All *in vitro* and *in vivo* experiments were repeated in triplicates. Data were analyzed using SPSS Software (version 20). Differences between data sets were tested using analysis of variance (ANOVA), followed by Tukey's post hoc test. In contrast, non-parametric ANOVA was used to compare the cytotoxic activity of the standard drug, unloaded nanocarrier, and niosomal IFO. A P-value < 0.05 was considered statistically significant.

3. Results

3.1. Physicochemical properties of niosomal IFO

The dynamic light scattering (DLS) method was used to examine the particle size and size distribution of niosomal IFO. Niosomal IFO was found to have a particle size of 97 ± 3.45 nm and a good dispersity index (PDI) of 0.214 (Fig. 2A). TEM imaging provided additional confirmation of the particle size of niosomal IFO. As can be observed in Fig. 2B, the particles appeared as small, white spherically shapes, with a diameter of approximately 80 to 100 nm. The particles showed no clear signs of agglomeration. The niosomal IFO further demonstrated high entrapment efficiency of 83.25 ± 2.54%.

3.2. Simulation results

3.2.1. Bilayer structure

A bilayer's area per lipid (APL) provides significant information about a bilayer or membrane due to its strong awareness of hydrophilic affinity amongst head groups and hydrophobic repulsion between non-polar hydrocarbon terminals. APL is also influenced by how head groups deal with water sources or aqueous solutions. Precise simulation estimation of additional structural characteristics, including lipid tail order parameters, bilayer thickness, electron density profiles, and general specific combination, follow naturally from accurate simulation prediction of the APL, which essentially means that

Table 1 The structural characteristics of Span 60, Tween 60, and cholesterol are compared before and after the MD simulation.

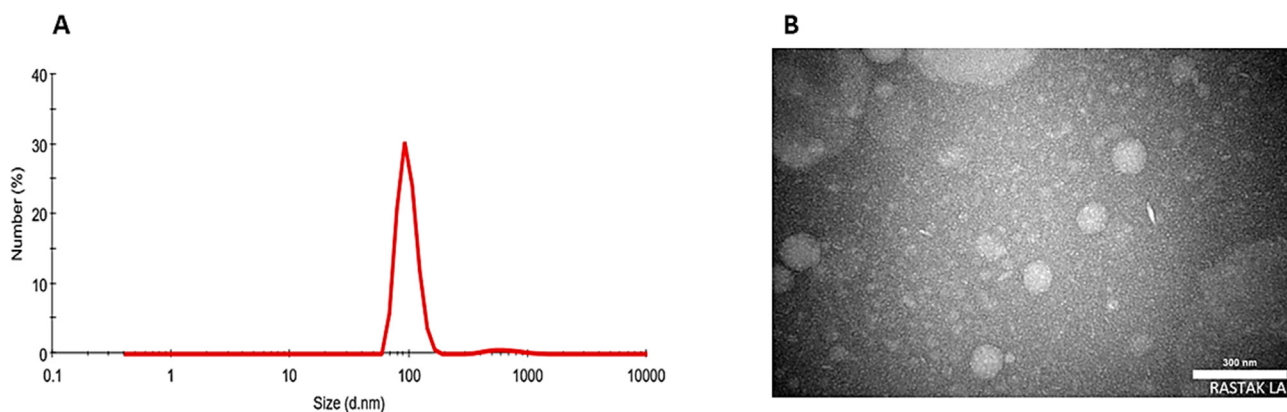| Lipid	Time	Area per lipid ($Å^2$)
Span 60	0 ns	74.0.1 ± 0.1
	140 ns	72.0 ± 0.1
Tween 60	0 ns	75.8 ± 0.1
	140 ns	74.1 ± 0.1
Cholesterol	0 ns	85.2 ± 0.1
	140 ns	83.4 ± 0.1

Fig. 2 A) Particle size distribution measured by DLS; B) TEM image of niosomal IFO.
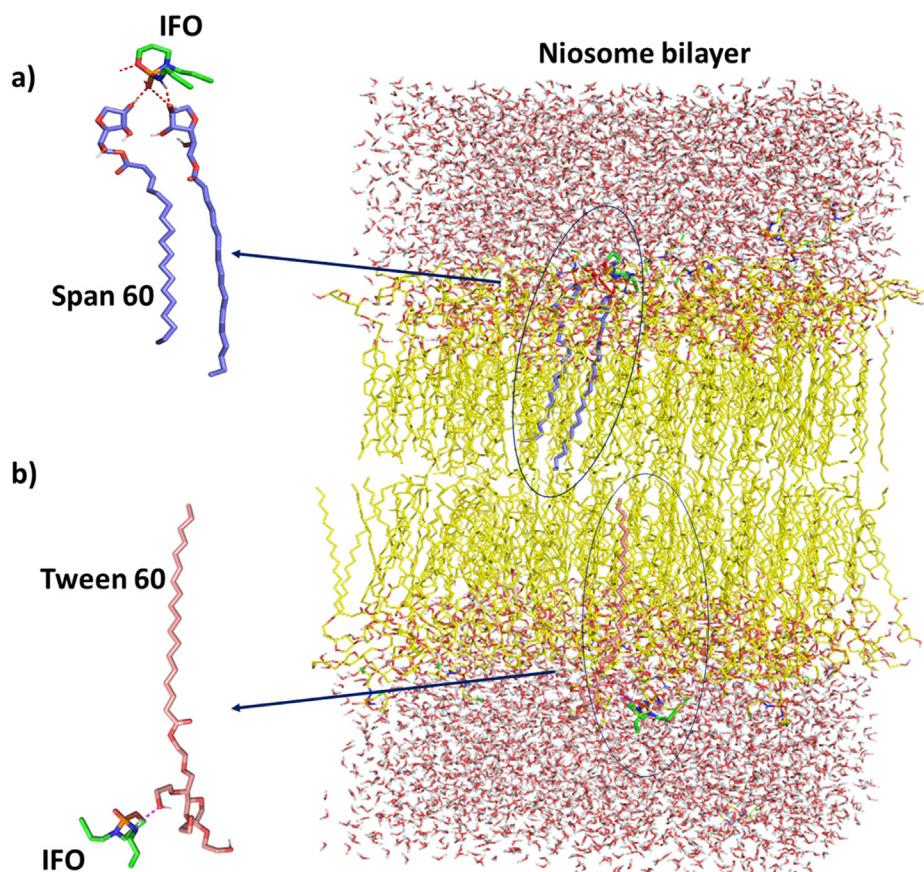
Fig. 3 Important interactions between IFO and Span 60/Tween 60 have been observed after MD simulation. (a) It is shown in the figure that significant interaction between nitrogen and oxygen atoms of IFO and Span 60 has been established. (b) Interactions have been observed between the structure of IFO and Tween 60. One of the most important of them is between the nitrogen atom of IFO and Tween 60.
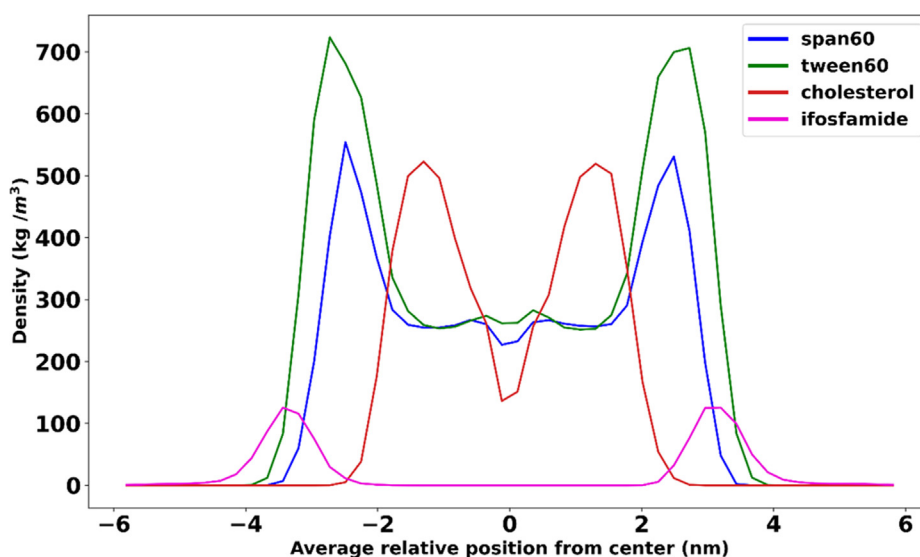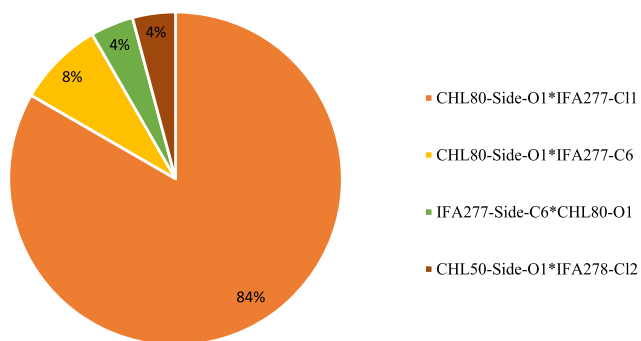

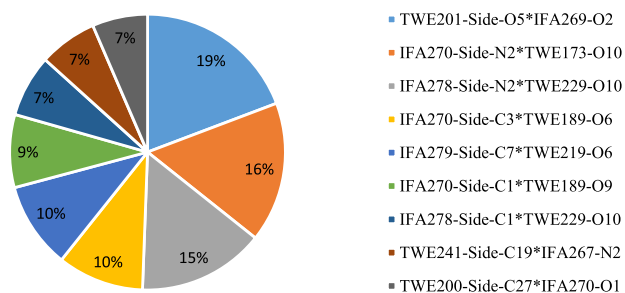**Fig. 4** Mass density profiles of cholesterol, span60, and tween60 in relation to z = 0.

the simulation's forecast of an exact 2-D density in the bilayer plane was true. Because lipids as well as self-assembling structures that resemble lipids mostly in bilayer regions, have slow-down conformational dynamics, precise estimation of an APL using MD simulations is computationally very expensive (Chaban and Prezhdo, 2014). Moreover, we multiplied the XY-surface area of the simulated box through the total cholesterol, Tween 60, and Span 60 in one leaflet to calculate the

Hydrogen bond- CHL

- CHL80-Side-O1*IFA277-Cl1
- CHL80-Side-O1*IFA277-C6
- IFA277-Side-C6*CHL80-O1
- CHL50-Side-O1*IFA278-Cl2

Z

- TWE201-Side-O5*IFA269-O2
- IFA270-Side-N2*TWE173-O10
- IFA278-Side-N2*TWE229-O10
- IFA270-Side-C3*TWE189-O6
- IFA279-Side-C7*TWE219-O6
- IFA270-Side-C1*TWE189-O9
- IFA278-Side-C1*TWE229-O10
- TWE241-Side-C19*IFA267-N2
- TWE200-Side-C27*IFA270-O1

Hydrogen bond- Span60

- SPA147-Side-O1*IFA267-O2
- SPA119-Side-O1*IFA268-O2
- SPA138-Side-O1*IFA279-O2
- SPA112-Side-O1*IFA271-O2
- SPA122-Side-O1*IFA282-O2
- SPA99-Side-O1*IFA270--O2
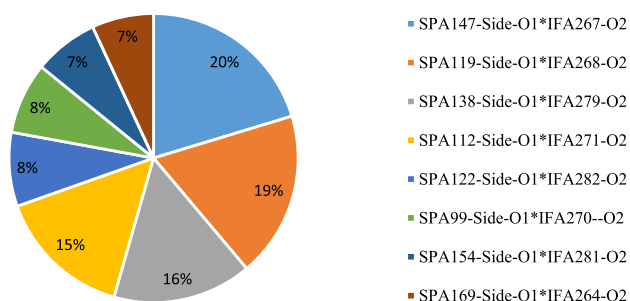- SPA154-Side-O1*IFA281-O2
- SPA169-Side-O1*IFA264-O2

Fig. 5 Typical and comprehensive hydrogen bond analysis formed by the substances IFO and Span 60, Tween 60, and cholesterol.

APL. The noisome bilayer component used in this work's structural characteristics, APL is compared in Table 1 for both the beginning and end of the simulation time.

In our niosomal model, the average APL for the span60 decreased at the start to the end of the MD simulation. When Tween 60 and cholesterol are added to tightly packed, high-order-oriented Span 60 bilayers, the bilayer does not grow at all. Important interactions between IFO and Span 60/Tween 60 have been observed after MD simulation, are shown in Fig. 3.

3.2.2. Mass density profiles

To explain the position and distribution of the span60, tween60, cholesterol, and IFO molecules in terms of the niosome bilayer molecules, we have calculated the mass density profiles. Each component's mass density profile concerning $z = 0$ is shown in Fig. 4. It shows that the bilayer equilibrated throughout the course if simulated, as evidenced by the symmetrical shape of the mass density profile along the z-axis. IFO's broad peak and low density demonstrate this molecule's propensity to remain at the interface of the water and span60 or tween60 headgroups. The absence of interaction between IFO and cholesterol is evident in this graph.

3.2.3. Order parameters

The order parameter is a measurement that can be made by experimentation using deuterium NMR. The formula for calculating SCD is given below, where yCD is the time-dependent angle between a C–H bond along an alkyl or acyl chain and the membrane normal (z-axis), and the brackets signify the average for both time and the entire ensemble.

3.2.4. Hydrogen bonding between noisome components and IFO

We used the hydrogen bond analysis throughout the 100 ns of trajectory to determine the quantity and/or length of hydrogen bonds created among three components of noisy bilayer-span60, Tween 60, and cholesterol with IFO. Using Gromacs 2020's H-bond tool, hydrogen bond patterns between the IFO and the lipids were determined. The H-bond formation threshold was 3.5 with a 30 angle.

Fig. 5 provides more information on the hydrogen bonding between IFO and span60, Tween 60, and cholesterol. In addition, the average number of hydrogen bonds is provided in Fig. 6. The results obtained from the hydrogen bond analysis show that the least effective interaction is between cholesterol and IFO, and the most interaction from the O1 atom side of cholesterol with the C atom of IFO. And further, as shown in Fig. 5, Span 60 has shown a greater tendency to have a hydrogen bond with IFO during MD simulation than with cholesterol. The results show that the role of the O1 atom related to Span 60 was high. Finally, the most tendency to create a hydrogen bond with IFO was related to Tween 60, where various parts of this structure were involved with a high contribution. In this type of interaction, the oxygen atoms of Tween 60 tend to bond with different parts of IFO, including the C and N atoms. As shown in Fig. 4, the O5 atom of Tween 60 and the N2 atom of IFO greatly contribute to creating hydrogen interaction. In addition, in the continuation of this analysis, it is shown in Fig. 6 belongs to the average hydrogen band, and the largest contribution is related to the hydrogen bond related to the Tween60 structure, which is shown in red color.

3.3. In vitro toxicity results

Both free and niosomal IFO exerted concentration-dependent cytotoxicity against the malignant cells, MCF7 and SH-SY5Y, after 48 h of exposure (Fig. 7). The standard IFO had an IC_{50} value of 4.483, 4.385, and 7.841μ g/mL in MCF7, SH-SY5Y, and HUVEC cells, correspondingly, indicating that the normal human cells derived from human umbilical veins were more resistant to IFO alone. Interestingly, niosomal IFO exhibited greater anticancer activity than standard IFO against malignant cells within the same incubation period ($IC_{50} = 0.410$ for MCF7 and 0.184μ g/mL for SH-SY5Y cells). Compared to untreated cells, both free and encapsulated drugs signifi-

cantly decreased the viability of HUVEC cells, with niosomal formulation being more toxic to them (7.841 vs. 3.724μ g/mL for standard and niosomal IFO, respectively). Niosomes that were not loaded with IFO had no toxic effects on the examined cell lines at concentrations below 1 μg/mL.

Compared with standard IFO, niosomal IFO has also induced more apparent morphological changes in MCF7 cancer cells, as can be seen in Fig. 8. Treatment of MCF7 cells with 1 μg/mL of free IFO, reduced the number of viable cells, while niosomal IFO caused the formation of apoptotic bodies when breast cancer cells were exposed to them at the same concentrations. Detached and rounded cells were abundantly observed in MCF cells exposed to 1 μg/mL of niosomal IFO.

3.4. In vivo findings

3.4.1. Biochemical results

In the present experiment, intravenous treatment with bulk IFO at (0.1 mg/kg) did not significantly change hepatic MDA content ($P > 0.05$), while significantly increased creatinine ($P < 0.05$), serum BUN ($P < 0.001$), serum ALT ($P < 0.001$) and serum AST levels ($P < 0.01$). Intravenous treatment with 0.2 mg/kg of bulk IFO significantly increased all serum parameters and lipid peroxidation ($P < 0.001$). Intravenous therapy with a low dose of niosomal IFO significantly increased serum parameters and liver MDA. Statistical analysis revealed a significant elevation of serum liver enzymes, kidney function markers, and hepatic MDA in rats treated with 0.2 mg/kg dose of niosomal IFO ($P < 0.05$, for all) (Table 2).

3.4.2. Histopathological examinations

The liver sections of the control group showed normal histological hepatic architecture, including well-preserved cytoplasm, prominent nucleus, and normal sinusoids (Fig. 9A). The liver section of rats treated with bulk IFO 0.1 mg/kg showed hepatocytes with a condensed nucleus, pyknotic hepatocytes, and dilated sinusoids (Fig. 9B). In rats treated with bulk IFO (0. 2 mg/kg), necrosis of hepatocytes and sinusoidal dilation were evident (Fig. 9C). Liver pathology images of the group receiving niosomal IFO (0.1) mg/kg showed normal sinusoids (Fig. 9D). In rats treated with (niosomal IFO 0.2 mg/kg), sinusoidal disarrangement (Fig. 9E) and hepatocytes necrosis of (Fig. 9F) with marked loss of architecture were observed.

Masson's trichrome-stained sections of the kidney cortex of normal control rats showed normal renal architecture, normal corpuscles, and renal tubules (Fig. 10A). In the renal cortex of the group receiving bulk IFO (0.1 mg/kg bw), signs of renal injury, including pyknotic hepatocytes, tubular atrophy, and tubular dilation, were present (Fig. 10B). Renal micrographs of rats receiving bulk IFO (0.2 mg/kg bw) showed collagen deposition and tubular atrophy (Fig. 10C). Kidney pathology images of the group receiving niosomal IFO (0.1) mg/kg bw showed congestion and decreased proximal tubule diameter (Fig. 10D). In kidney sections of the group treated with niosomal IFO (0.2 mg/kg bw), fibrosis, inflammatory cell infiltration (Fig. 10E), and extracellular matrix accumulation were the main histopathological lesions (Fig. 10F).

4. Discussion

In order to improve drug delivery while minimizing undesirable side effects, we developed a novel niosomal formulation with Span 60 and Tween 60 as the IFO carrier in this study. To the best of our knowledge, this is the first report attempting to design IFO-loaded niosomes and evaluate their biological effects through different in vitro, in vivo, and in silico assessments. Span 60 and Tween 60 are commonly used surfactants in niosome preparation due to their amphiphilic nature and biocompatibility. These surfactants have a hydrophilic head and a hydrophobic tail, which allows them to form stable bilayer structures in water. The choice of these surfactants is based on several factors, including their ability to form stable niosomes, their biocompatibility, and their low toxicity. Span 60 has a high HLB (Hydrophilic-Lipophilic Balance) value, which makes it suitable for forming niosomes with a high ratio of hydrophilic to lipophilic components. Tween 60, on the other hand, has a lower HLB value, which makes it suitable for forming niosomes with a higher ratio of lipophilic to hydrophilic components (Junyaprasert et al., 2012; Basiri et al., 2017). Using the DLS method, niosomal IFO was found to have particles that were 97 $\pm$ 3.45 nm in size and had an outstanding PDI of 0.214. (Fig. 2A). It has frequently been observed that the increased permeability and retention (EPR) effect can cause tiny particle sizes of < 200 nm to concentrate preferentially in tumor tissues. Aside from this, tiny particles might successfully bypass the blood circulation's RES-based clearing mechanism (Chen et al., 2015). As seen in Fig. 2B and based on TEM images, diameter of loaded formulation was in the range of 80–100 nm. However, the TEM image is not clear enough to determine the exact shape of the particles, and it is difficult to distinguish individual particles from each other. It must be noticed that the TEM particle size was smaller than the DLS analysis particle size. The distinction in particle size between the hydrated state (from DLS) and dry state (from TEM) of the particles may be the cause. The Niosomal IFO further demonstrated a high entrapment efficacy of 83.2 5 $\pm$ 2.54%. Based on a nanoparticle delivery system's encapsulation efficiency (EE) values, its potential may be forecasted (García-Manrique et al., 2020). IFO has been reported to be enclosed in a variety of nanocarriers by several writers. To increase the antitumor effectiveness in osteosarcoma, for instance, IFO-loaded poly (lactic-co-glycolic acid) PLGA-dextran polymeric nanoparticles were created with an EE of 89% (Chen et al., 2015). Additionally, it has been observed that IFO-loaded lipid-core nanocapsules with an EE of 93.25% improved the anticancer activity in MG63 osteosarcoma cells. The size and structure of the nanocarriers determine the variations in EE% between various nanocarriers (Wang et al., 2018).

In the in-silico part of this study, the APL of Span 60, Tween 60, and cholesterol were examined through the MD course. According to our results, this value reached 72.0 $\pm$ 0.1, 74.0 $\pm$ 0.1, and 83.0 $\pm$ 0.1 Å^2 after 140 ns MD simulation. The mass density profile of IFO molecules immersed in water at the top and bottom of the bilayer showed that they tried to reside at the interface of water/Tween60 and water /Span60 rather than penetration into the bilayer by strong interaction with their headgroups. In addition, we have
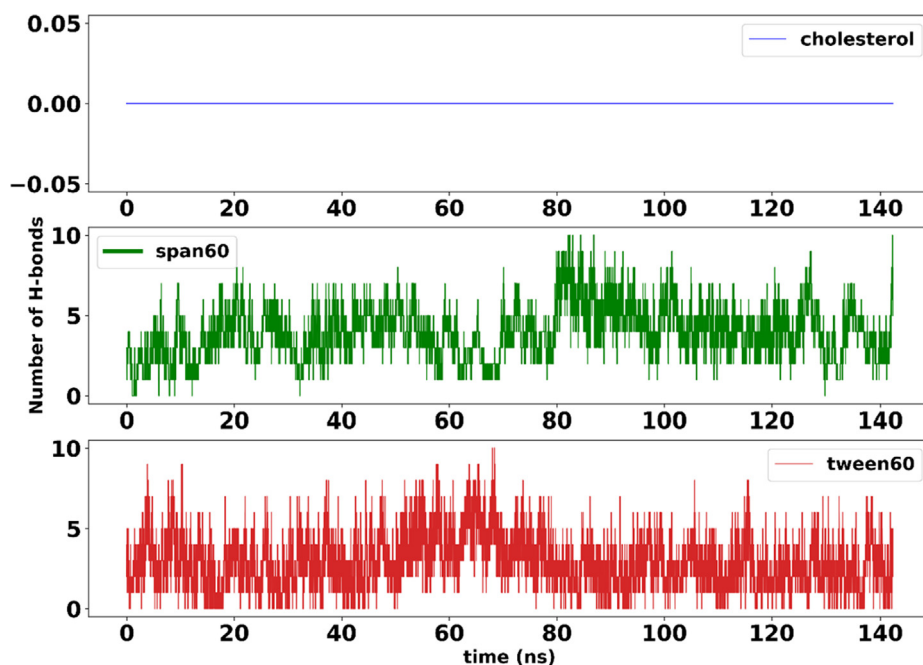
Fig. 6   Average hydrogen bond analysis of IFO with Span 60, Tween 60, and cholesterol in the current simulation.
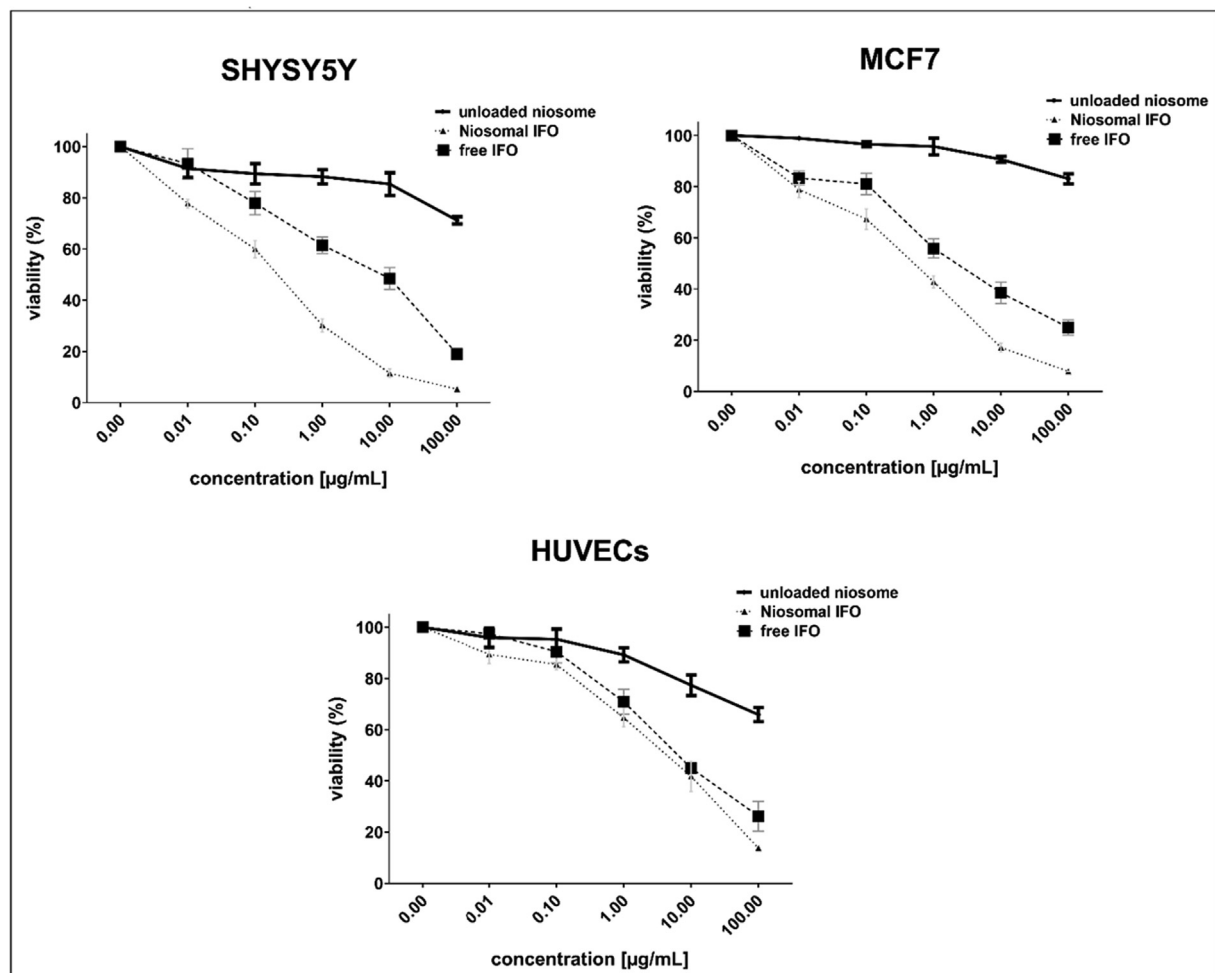

Fig. 7   Growth inhibitory effects of free and encapsulated IFO against malignant and non-malignant human cells after 48 h of exposure.
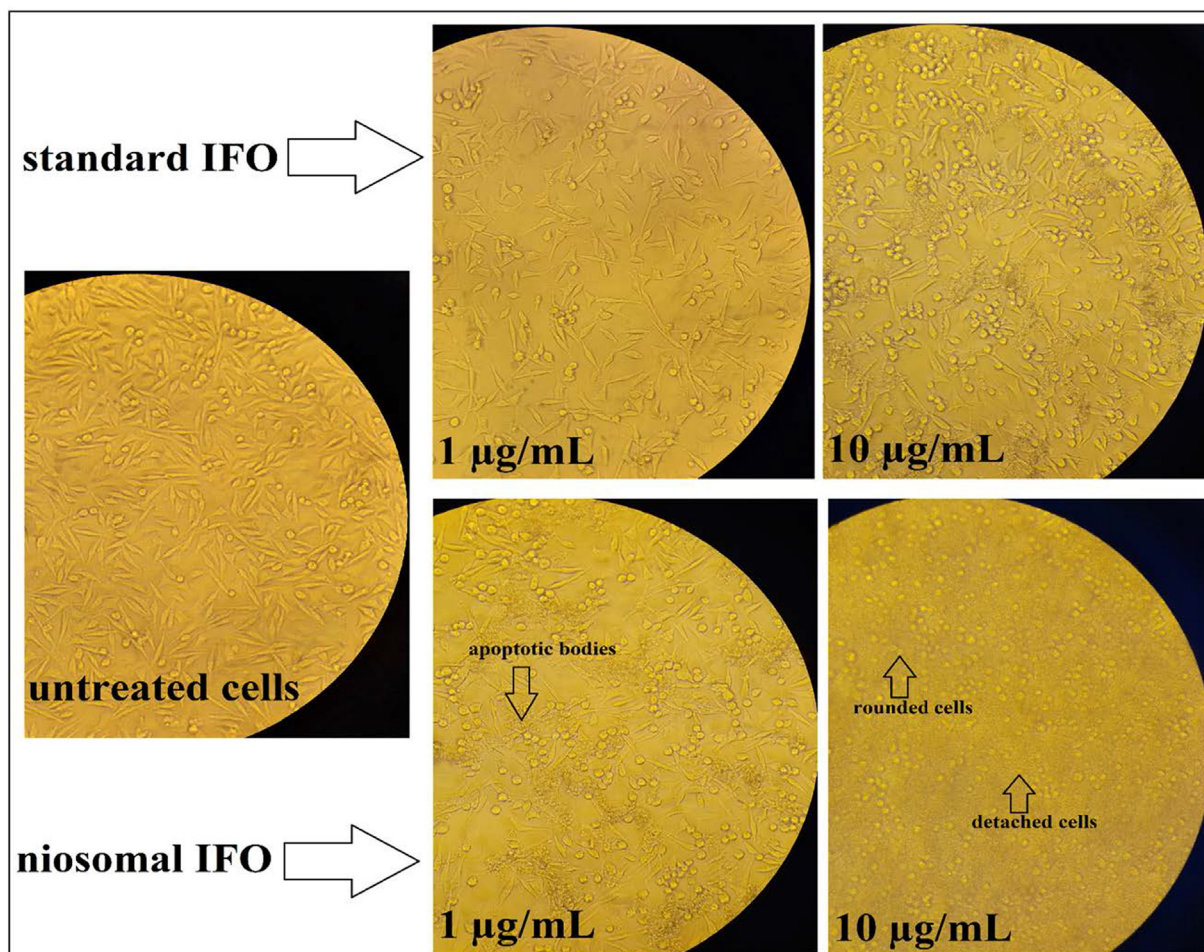
Fig. 8 Microscopic images of MCF7 cells treated with 1 and 10 µg/mL of standard and niosomal IFO for 48 h.

Table 2 Serum AST, ALT, BUN, creatinine, and liver MDA of the groups.

Parameter	Control	Bulk IFO 0.1 mg/kg	Bulk IFO 0.2 mg/kg	Niosomal IFO 0.1 mg/kg	Niosomal IFO 0.2 mg/kg
Creatinine (mg/dL)	0.7 ± 0.14	$1.18* \pm 0.21$	$2*** \pm 0.38$	$1.0* \pm 0.19$	$1.8*** \pm 0.36$
BUN (mg/dL)	7.3 ± 2.1	$17.2*** \pm 5.1$	$17.5*** \pm 2.1$	$11.8* \pm 1.9$	$16.1*** \pm 3.0$
ALT (U/L)	37.6 ± 3.6	$82.3*** \pm 16.5$	$137.5*** \pm 29.0$	$69.8* \pm 19.9$	$148.1*** \pm 16.7$
MDA (nmol/mg protein)	37.7 ± 9	41.2 ± 7.7	$92.7*** \pm 14.4$	$66.1* \pm 4.8$	$100.6*** \pm 16.6$
AST (U/L)	38.0 ± 9.4	$64.2** \pm 18.2$	$134.5*** \pm 18.3$	$70.6* \pm 10.4$	$144.2*** \pm 16.8$

* Significantly different as compared with the control group, ($p < 0.05$).
** *Significantly* different *as compared with the control group, ($p < 0.01$).*
*** *Significantly* different *as compared with the control group, ($p < 0.001$).*

not seen any contact between the drug and the cholesterol molecules. We also investigate the stability of IFO molecules in the vicinity of the lipid bilayer. According to this investigation, this stability stems from the strong hydrogen bonds between nitrogen and oxygen atoms connected to phosphor in IFO with Span 60 and Tween 60 headgroups.

There have been many studies on the co-delivery of IFO and other anticancer agents to treat cancer. For example, Saimi et al. developed a niosomal formulation for the co-entrapment of IFO and cisplatin for lung cancer treatment (Mohamad Saimi et al., 2021). Similarly, Cosco and colleagues

encapsulated IFO and tamoxifen within liposomes, as multidrug carriers and investigated their antitumor efficacy against breast cancer cells (Cosco et al., 2012). In vitro cytotoxicity results suggested that niosomes could be useful nanotools for carrying IFO to cancer cells; nevertheless, the safety of such formulations concerning non-cancerous cells and tissues must be investigated further. It has been established that IFO has an average half-life of 20 h, corresponding to pH values of 4 and 9. Even though IFO degradation is relatively independent of pH, proton or hydroxyl catalysis occurs at extreme pH values (Kaijser et al., 1991). IFO metabolization primarily occurs
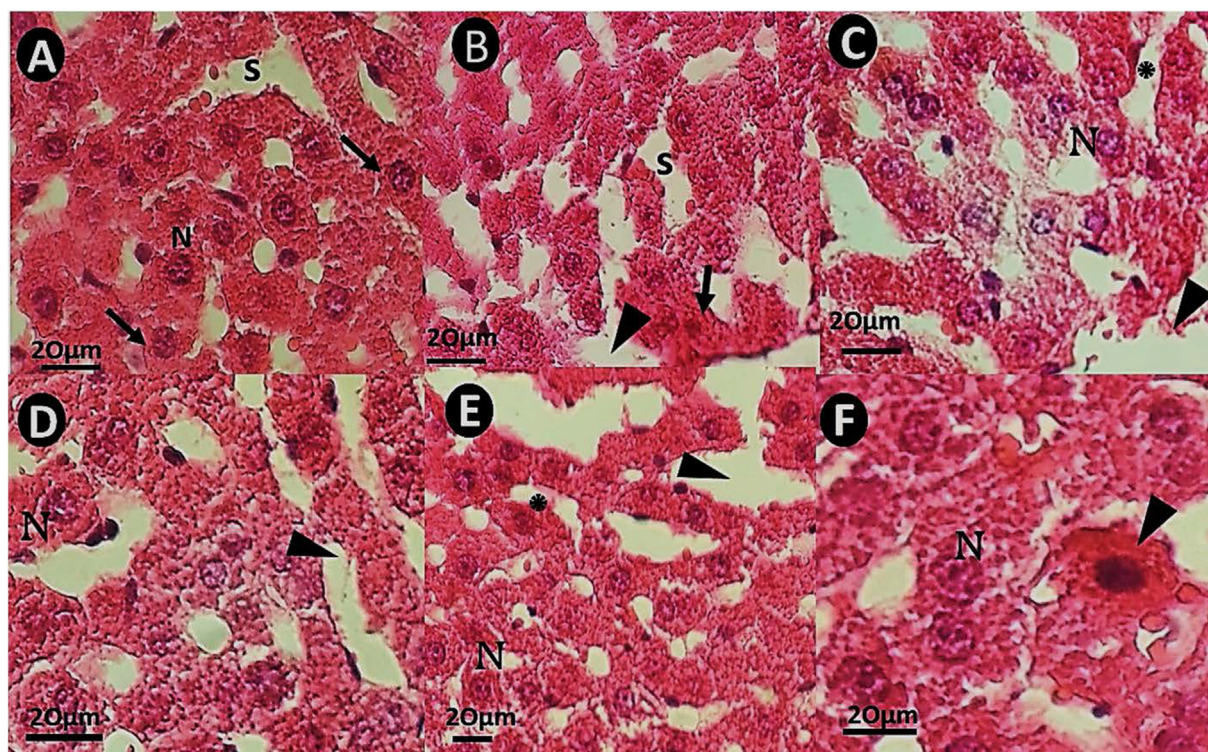
Fig. 9 H&E staining pathology images of rat liver tissues (×40). The scale bar represents 20 μm. (**A**): hepatic section of a rat from control, with normal liver tissue and normal sinusoids (S); (**B**): hepatic micrograph of a rat received bulk IFO 0.1 mg/Kg, with pyknotic hepatocytes (arrow) and dilated sinusoids (arrowhead) without fibrosis; (**C**): hepatic section of a rat treated with bulk IFO 0.2 mg/kg. The arrow shows sinusoidal dilation; (**D**): Liver pathology images of a rat that received niosomal IFO (0.1 mg/kg showing normal sinusoids (arrowhead); (**E**): sinusoidal disarrangement in rats treated with niosomal IFO 0.2 mg/kg. (E&F: liver sections of rats treated with niosomal IFO 0.2 mg/kg) (**F**): necrosis of hepatocytes (arrowhead) and cytoplasmic condensation in rats treated with niosomal IFO 0.2 mg/kg.

in the liver (Hill et al., 1973). Oral and intravenous administration have different preferential metabolic pathways. The prodrug is transformed by cytochromes into an intermediate derivative known as 4-OH-IFO, which is in equilibrium with its tautomeric form. As a result of the release of urotoxic acrolein, aldoifosfamide spontaneously breaks down to IFO (Verdeguer et al., 1989). According to Aleksa et al. observation, liver injury, oxidative stress, and inflammation resulted from IFO injection (Aleksa et al., 2005). In a new study, male rats receiving IFO showed severe hepatic dysfunction and increased aminotransferases (Özdemir et al., 2022). Our results showed that treatment with free IFO and niosomal IFO significantly increased hepatic aminotransferases and induced hepatocyte necrosis. The current study showed mild elevation of serum liver enzymes which can be considered an adverse effect of IFO. In our current work, ALT to AST ratio was nearly equal to one, which is a sign of drug-related liver damage. Histopathological findings showed necrosis in the liver and kidney of rats. The current results were in-line with the findings of Cheung et al. (Cheung et al., 2011). Moreover, our observations were in line with biochemical results. In severe cases, IFO neurotoxicity can cause comas and death due to its psychiatric and neurological effects (Kerbusch et al., 2001). A previous study conducted by Vakiti et al. reported metabolic encephalopathy in two patients with cutaneous T-

Cell lymphoma. Chloroacetaldehyde levels in plasma cause acetyl-CoA dehydrogenase to become inactive, inhibiting mitochondrial oxidative phosphorylation and brain glutathione levels (Vakiti et al., 2018).

Chemotherapeutic agents, including IFO, might lead to hepatotoxicity symptoms. It is usually possible to manage chemotherapy-induced liver injury by closely monitoring liver function tests for signs of liver injury and by reducing the dose of the anticancer agent (Barani et al., 2023). Nanocarriers have been designed to overcome this therapeutic hurdle to improve anticancer agents' delivery, such as IFO, to tumor cells. In our work, we have loaded IFO within a nanoniosomal formulation made of span 60 and tween 80. Span 60 is a common, nonirritant, safe, and available nonionic surfactant (Arellano et al., 1998). The chemical is documented to be non-hazardous and has been proven safe for external application to the eye (Basha et al., 2013). On the other hand, Tween 80, a synthetic nonionic surfactant, is widely used as an excipient in drug formulation (Schwartzberg and Navari, 2018). This chemical was found to be safe for use in intravenous and inhaled medications (Kopec et al., 2008). In order to assess possible undesirable effects of our formulation, normal human umbilical vein endothelial cells (HUVECs) were exposed to an escalating concentration of unloaded nanoniosome dispersions, and found that the unloaded niosomes did not induce any toxic effects
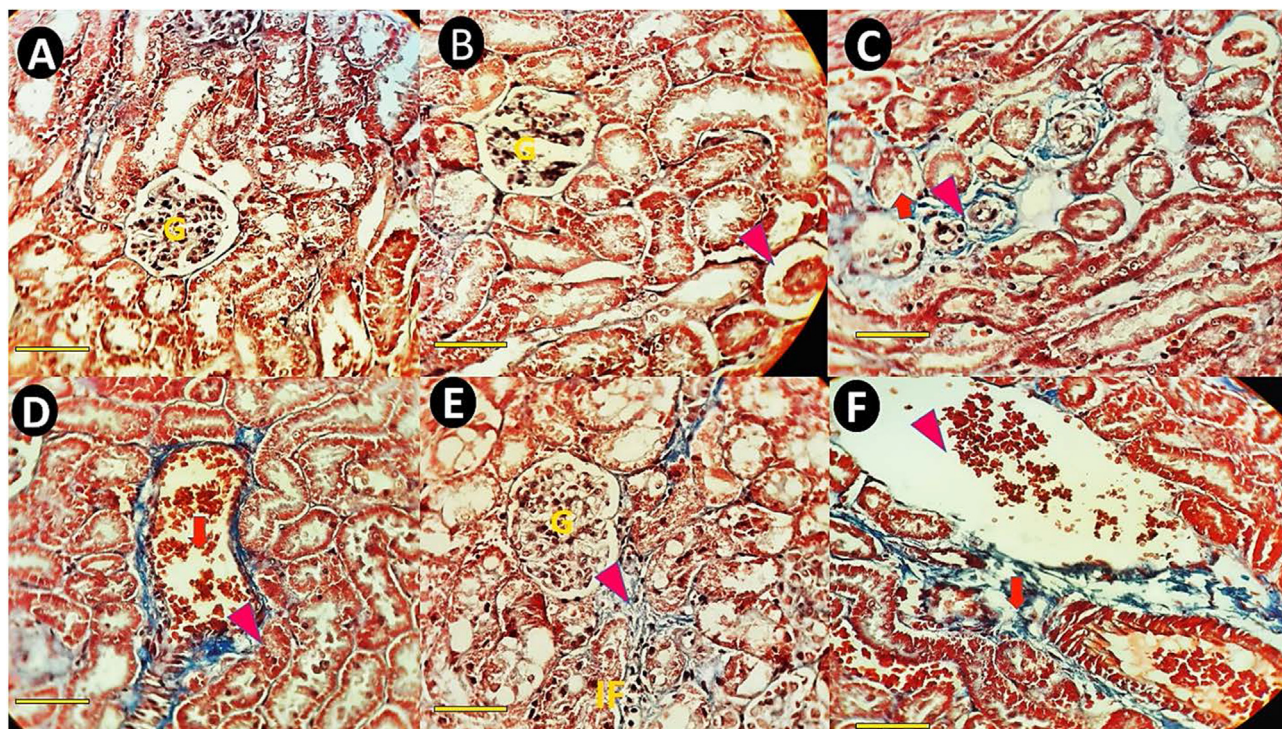
Fig. 10 Masson's trichrome–stained sections of rat kidney cortex (×40). The scale bar represents 100 μm. (A) A representative kidney section from a normal control rat's cortex shows normal renal architecture, normal corpuscles (G), and renal tubules. (B) Renal cortex of a rat received bulk IFO (0.1 mg/kg bw) with normal glumerole. (C) Kidney section of a rat treated with bulk IFO (0.2 mg/kg bw). The arrowhead shows kidney collagen deposition, and the arrowhead shows tubular atrophy. (D) Kidney pathology images of a rat that received niosomal IFO (0.1 mg/kg bw) showing congestion (arrow) and decreasing the proximal tubule diameter (arrowhead). (E&F, kidney sections of rats treated with niosomal IFO (0.2 mg/kg bw) (E) Fibrosis (arrow) and inflammatory cells infiltration (IF) in rats treated with niosomal IFO (0.2 mg/kg bw). (F) Kidney section of a rat treated with niosomal IFO (0.2 mg/kg bw). The arrow shows extracellular matrix accumulation.

against these cells. However, the safety profile of the developed formulation should be further studied in other non-cancerous human tissues as well.

In vivo experiments were reported to show the potential side effects of IFO, including neurotoxicity, nephrotoxicity, and hepatotoxicity (Banh et al., 2022). Such experiments are required to monitor, understand, and predict the pharmacokinetics and potential toxicity of IFO as a chemotherapy agent. Most of the in vivo studies used mice (AlMotwaa et al., 2020) and rats (Çelik et al., 2020), and a few studies used rabbits (Mousa et al., 2022) as experimental animals. Renal dysfunction is also another risk factor due to the accumulation of IFO during renal insufficiency (Dollery, 1999). Renal toxicity is one of the main side effects of IFO. A study by Burk et al. reported that treatment with IFO has led to renal tubular Fanconi syndrome in five patients with Wilms tumor (Burk et al., 1990). In our histopathological work, rats treated with IFO showed severe histological lesions, including congestion, collagen deposition, and inflammatory cell infiltration, which was in line with the results of springate et al. (Springate and Van Liew, 1995). Nakata et al. showed that using Span 80 vesicles for the drug delivery system can reduce kidney damage caused by IFO (Nakata et al., 2015). Further confirmation was achieved by Velmurugan et al., who used a nephrotoxicity model of IFO in animal life to evaluate the protective effects of IFO-loaded NLC. The administration of IFO_NCL reduces

the risk of kidney disorders or side effects caused by IFO because it prevents serum creatinine levels (47.82 ± 2.25 vs. 32.64 ± 1.28 mmol l − 1) from increasing and reduces microglobulin ß2 (25.54 ± 122 vs. 19.86 ± 1.22 nmol l − 1) and magnesium excretion (19.62 ± 1.56 vs. 16.12 ± 1.22 mm ol l − 1) (Velmurugan and Nair, 2018).

A formulation for oral delivery of IFO was also developed by Velmurugan et al. It was made by coating nanostructured lipid carriers (NLCs) with hydrophobic polymers (sodium alginate and chitosan). A ratio of drug to lipid of 1:3, a ratio of organic to the aqueous phase of 1:10, and 1 % w/v surfactant were found to be the optimal formulation. Under optimized conditions, the IFO nanostructured lipid carrier had a 77 % entrapment efficiency, 6.14 % drug loading, a diameter of 223 nm, and a −25 mV zeta potential. It was determined that the delivery system released IFO over a period of 72 h with improved stability, high entrapment efficiency, and sustained release from this nanostructured lipid carrier (Velmurugan and Selvamuthukumar, 2016). Similarly, in a study, IFO-NLCs were made by crosslinking chitosan with sodium alginate using solvent diffusion and were shown to be effective against Dalton's ascitic lymphoma (DAL). Compared with IFO suspension, IFO from NLC showed a sixfold higher relative bioavailability, which resulted in a 35 % increase in survival time after IFO-NLC administration. Additionally, IFO-NLC has a bioavailability of 632.86 % (Velmurugan and

Selvamuthukumar, 2014). Panit et al. developed solid lipid nanoparticles (SLNs) modified on the surface to improve the stability and sustainability of IFO release. Chitosan and GMO SLNs were prepared using the double emulsion method and crosslinked with sodium tripolyphosphate before lyophilization under different vacuum pressures. Experimentally, we found that the particles loaded drugs at $98.37 \pm 10.9\%$ (n = 3). After 24 h, approximately 70% of the drug released from the delivery systems had been released. SLNs demonstrated high IFO uptake and permeability for Caco-2 cells and enhanced stability and sustained release (Pandit and Dash, 2011).

Our newly designed nanovehicle was not functionalized; however, our findings showed that it could deliver IFO to cancer cells in an efficient manner; hence, it might be safe to say that IFO-loaded niosomes efficiently targeted cancer cells. This is evidenced by the results of the MTT assay, where it was found that both free and niosomal IFO resulted in significant cell death in cancerous cells MCF7 and SH-SY5Y. Our formulation exerted greater cell-killing effects than standard IFO (indicated by lower IC_{50}s) than standard IFO. We believe that encapsulating IFO in niosomal structures enhances the drug's cell growth inhibition effects and controls its release in proximity to the tumor. A higher tumor uptake was seen after 48 h of treatment, possibly due to IFO's enhanced permeability and retention (EPR) effect, thereby substantially enhancing its anticancer activity. Because of the EPR properties of nanoparticle-based delivery systems, cancer therapy can be significantly impacted by the passive accumulation properties of nanoparticle-based delivery systems (Zhao et al., 2018). Accordingly, the nanosized niosomal formulation is believed to be more effective at diffusing into tumor cells via the EPR effect (Fang, 2022). Targeted delivery of IFO has significantly increased IFO accumulation in breast and brain cancer cells. Therefore, the lower IC_{50} value of niosomal IFO compared to the standard drug is explained by the fact that a lower concentration of IFO is required to exert the same toxicity.

Since most of the drugs are lipophilic, the drug's solubility and biocompatibility with lipids are among the most important aspects of formulation as NLCs and SLCs. Due to partitioning effects, this nanocarrier has a low drug-loading capacity (Salvi and Pawar, 2019; Kaul et al., 2018). Therefore, oral delivery of hydrophilic drugs is done using hydrophilic polymers, such as alginate and chitosan. Because the drug diffuses rapidly into the external aqueous phase and has a low entrapment efficiency, formulation scientists find it challenging to prepare nanoparticles for hydrophilic drugs (Liu et al., 2010). IFO is a highly hydrophilic drug, so preparing a nanoformulation with high drug loading efficiency based solely on the lipid phase alone is extremely difficult. In this context, Sharma et al.'s study showed that niosomes could be used to deliver both hydrophilic (Dox) and hydrophobic (curcumin) drugs, demonstrating their potential to be used in anticancer treatments. It has been estimated that curcumin and Dox encapsulate about 90% and 25% of their encapsulation efficiency, respectively, in the aqueous lipid bilayer cores and outer lipid bilayer shells, respectively, where they accumulate (Sharma et al., 2015). Therefore, niosomes with a hydrophilic compartment can be considered effective IFO drug carrier without a hydrophilic polymer coating.

Some limitations, including physical instabilities, aggregation, fusion, leaking of the entrapped drug, its rapid degradation, and lack of human safety data, might restrict the application niosomes for effective IFO delivery. Despite these disadvantages, niosomes have several benefits over liposomes, including lower synthesis costs, greater stability, and more. Additionally, niosomes can entrap many cargo types within their multi-environmental structure, demonstrating their applicability in treating a wide variety of diseases through various routes of drug delivery. In our study, entrapping IFO in well-characterized niosomes showed promise in our study for future application in drug delivery. Unfortunately, there were several drawbacks to our study. First, we were unable to identify the mechanism by which niosomal IFO inhibits tumor growth. The second issue is that the *in vivo* and *in vitro* toxicity tests were only conducted on a small sample of tissues and cell types. Finally yet importantly, the novel formulation needs to be evaluated for its potential to inhibit the development of certain cancers.

5. Conclusion

In the present study, we designed niosomal IFO, characterized the formulation, and investigated its anticancer activity against cancerous cell lines. The drug-loaded formulation was characterized in terms of size distribution, morphology, drug loading, dynamic simulation, cytotoxicity assay, and *in vivo* analysis. The niosomal IFO showed a nanometric size range with a high drug-loading capacity. This property is important for all biomedical applications, including cancer chemotherapy. Biochemical and histopathological examination showed dose-dependent toxicity of niosomal IFO and free IFO. Moreover, the ALT/AST ratio examination showed drug-induced toxicity, confirmed by histopathological findings. The theoretical examination illustrated that the main interaction of IFO immersed into the niosome is due to its nitrogen and oxygen atoms connected to phosphor with Span60 and Tween60 headgroups.

Our formulation exhibited optimum size, with desirable anticancer activity, and can be considered a promising carrier with a high potential for future usage; however, more studies are needed to assess its safety towards normal human cells. Our study provides a scientific basis for additional studies into noisome entrapment efficiency as a potentially useful carrier of chemotherapeutic drugs for overcoming pharmacokinetic limitations.

7. Institutional review board statement

The protocol of the present study was approved by the local ethic committee of Zahedan University of Medical Sciences (Ethical code: IR.ZAUMS.REC.1400.333). The webpage for the ethical certificate is available at https://ethics.research.ac.ir/EthicsProposalViewEn.php?id = 239112.

CRediT authorship contribution statement

Mohammad Reza Hajinezhad: Writing – review & editing, Writing – original draft, Resources, Investigation. **Sheida Shahraki:** Supervision, Writing – review & editing, Resources,

Methodology, Conceptualization. **Zahra Nikfarjam:** Writing – review & editing. **Fatemeh Davodabadi:** Writing – original draft. **Shekoufeh Mirinejad:** Investigation, Writing – original draft. **Abbas Rahdar:** Methodology. **Saman Sargazi:** Investigation, Conceptualization, Methodology, Supervision, Writing – review & editing. **Mahmood Barani:** Supervision, Writing – review & editing, Writing – original draft, Resources, Methodology, Investigation.

Declaration of Competing Interest

The authors declare that they have no known competing financial interests or personal relationships that could have appeared to influence the work reported in this paper.

References

Aleksa, K., Matsell, D., Krausz, K., Gelboin, H., Ito, S., Koren, G., 2005. Cytochrome P450 3A and 2B6 in the developing kidney: implications for ifosfamide nephrotoxicity. Pediatr. Nephrol. 20, 872–885.

Alexander, R.L.; Behme, R.J.; Scott, J.A.; Brooke, D. Lyophilized ifosfamide compositions. (1993).

AlMotwaa, S.M.; Alkhatib, M.H.; Alkreathy, H.M. Incorporating ifosfamide into salvia oil-based nanoemulsion diminishes its nephrotoxicity in mice inoculated with tumor. *BioImpacts: BI* 10 (2020) 9.

Arellano, A., Santoyo, S., Martn, C., Ygartua, P., 1998. Surfactant effects on the in vitro percutaneous absorption of diclofenac sodium. Eur. J. Drug Metab. Pharmacokinet. 23, 307–312.

Baillie, A., Florence, A., Hume, L., Muirhead, G., Rogerson, A., 1985. The preparation and properties of niosomes—non-ionic surfactant vesicles. J. Pharm. Pharmacol. 37, 863–868.

Banh, C., Valsvik, K., Arredondo, A., Notbohm, K., Elquza, E., Babiker, H., Kraft, A., Boiles, A.R., Persky, D., Ortega, A., 2022. Transitioning ifosfamide chemotherapy regimens to the ambulatory setting: reviewing cost savings and safety profile. Support. Care Cancer 30, 2755–2766.

Barani, M., Mukhtar, M., Rahdar, A., Sargazi, S., Pandey, S., Kang, M., 2021. Recent advances in nanotechnology-based diagnosis and treatments of human osteosarcoma. Biosensors 11, 55.

Barani, M., Hajinezhad, M.R., Zargari, F., Shahraki, S., Davodabadi, F., Mirinejad, S., Sargazi, S., Rahdar, A., Díez-Pascual, A.M., 2023. Preparation, characterization, cytotoxicity and pharmacokinetics of niosomes containing gemcitabine: In vitro, in vivo, and simulation studies. J. Drug Delivery Sci. Technol. 84, 104505.

Basha, M., Abd El-Alim, S.H., Shamma, R.N., Awad, G.E., 2013. Design and optimization of surfactant-based nanovesicles for ocular delivery of Clotrimazole. J. Liposome Res. 23, 203–210.

Basiri, L., Rajabzadeh, G., Bostan, A., 2017. Physicochemical properties and release behavior of Span 60/Tween 60 niosomes as vehicle for α-Tocopherol delivery. LWT 84, 471–478.

Berendsen, H.J.; Postma, J.v.; Van Gunsteren, W.F.; DiNola, A.; Haak, J.R. Molecular dynamics with coupling to an external bath. *The Journal of chemical physics* 81 (1984) 3684-3690.

Berendsen, H.J., van der Spoel, D., van Drunen, R., 1995. GROMACS: A message-passing parallel molecular dynamics implementation. Comput. Phys. Commun. 91, 43–56.

Bhardwaj, P., Tripathi, P., Gupta, R., Pandey, S., 2020. Niosomes: A review on niosomal research in the last decade. J. Drug Delivery Sci. Technol. 56, 101581.

Burk, C.D., Restaino, I., Kaplan, B.S., Meadows, A.T., 1990. Ifosfamide-induced renal tubular dysfunction and rickets in children with Wilms tumor. J. Pediatr. 117, 331–335.

Cancer. Available online: https://www.who.int/news-room/fact-sheets/detail/cancer (accessed on.

Case, D.; Pearlman, D.; Caldwell, J. Amber 18.(2018) University of California. *San Francisco*.

Çelik, H., Kucukler, S., Çomaklı, S., Özdemir, S., Caglayan, C., Yardım, A., Kandemir, F.M., 2020. Morin attenuates ifosfamide-induced neurotoxicity in rats via suppression of oxidative stress, neuroinflammation and neuronal apoptosis. Neurotoxicology 76, 126–137.

Chaban, V.V., Prezhdo, O.V., 2014. Computationally efficient prediction of ionic liquid properties. J. Phys. Chem. Lett. 5, 1973–1977.

Chen, F., Smith, P.E., 2007. Simulated surface tensions of common water models. J. Chem. Phys. 126, 221101.

Chen, B., Yang, J.-Z., Wang, L.-F., Zhang, Y.-J., Lin, X.-J., 2015. Ifosfamide-loaded poly (lactic-co-glycolic acid) PLGA-dextran polymeric nanoparticles to improve the antitumor efficacy in Osteosarcoma. BMC Cancer 15, 1–9.

Cheung, M., Jones, R.L., Judson, I., 2011. Acute liver toxicity with ifosfamide in the treatment of sarcoma: a case report. J. Med. Case Rep. 5, 1–5.

Cosco, D., Paolino, D., Cilurzo, F., Casale, F., Fresta, M., 2012. Gemcitabine and tamoxifen-loaded liposomes as multidrug carriers for the treatment of breast cancer diseases. Int. J. Pharm. 422, 229–237.

Danhier, F., Feron, O., Préat, V., 2010. To exploit the tumor microenvironment: passive and active tumor targeting of nanocarriers for anti-cancer drug delivery. J. Control. Release 148, 135–146.

Dickson, C.J., Madej, B.D., Skjevik, Å.A., Betz, R.M., Teigen, K., Gould, I.R., Walker, R.C., 2014. Lipid14: the amber lipid force field. J. Chem. Theory Comput. 10, 865–879.

Dollery, C.S., 1999. Therapeutic drugs. Churchill Livingstone.

Fang, J. EPR effect-based tumor targeted nanomedicine: A promising approach for controlling cancer. (2022) 12 95.

Gao, Y.; K Shen, J.; Milane, L.; J Hornicek, F.; M Amiji, M.; Duan, Z. Targeted cancer therapy; nanotechnology approaches for overcoming drug resistance. *Current Medicinal Chemistry* 22 (2015) 1335-1347.

García-Manrique, P., Machado, N.D., Fernández, M.A., Blanco-López, M.C., Matos, M., Gutiérrez, G., 2020. Effect of drug molecular weight on niosomes size and encapsulation efficiency. Colloids Surf. B Biointerfaces 186, 110711.

Ghaznavi, H., Shirvaliloo, M., Zarebkohan, A., Shams, Z., Radnia, F., Bahmanpour, Z., Sargazi, S., Saravani, R., Shirvalilou, S., Shahraki, O., 2021. An updated review on implications of autophagy and apoptosis in tumorigenesis: possible alterations in autophagy through engineered nanomaterials and their importance in Cancer therapy. Mol. Pharmacol. 100, 119–143.

Giraud, B., Hebert, G., Deroussent, A., Veal, G.J., Vassal, G., Paci, A., 2010. Oxazaphosphorines: new therapeutic strategies for an old class of drugs. Expert Opin. Drug Metab. Toxicol. 6, 919–938.

Gu, Z., Da Silva, C.G., Van der Maaden, K., Ossendorp, F., Cruz, L. J., 2020. Liposome-based drug delivery systems in cancer immunotherapy. Pharmaceutics 12, 1054.

Harati-Sadegh, M., Sargazi, S., Saravani, M., Sheervalilou, R., Mirinejad, S., Saravani, R., 2021. Relationship between miR-143/145 cluster variations and cancer risk: proof from a Meta-analysis. Nucleosides Nucleotides Nucleic Acids 40, 578–591.

Hill, D.L., Laster Jr, W.R., Kirk, M.C., Dareer, S.E., Struck, R.F., 1973. Metabolism of Iphosfamide [2-(2-chloroethylamino)-3-(2-chloroethyl) tetrahydro-2 H-1, 3, 2-oxazaphosphorine 2-oxide] and production of a toxic Iphosfamide metabolite. Cancer Res. 33, 1016–1022.

Junyaprasert, V.B., Teeranachaideekul, V., Supaperm, T., 2008. Effect of charged and non-ionic membrane additives on physicochemical properties and stability of niosomes. AAPS PharmSciTech 9, 851–859.

Junyaprasert, V.B., Singhsa, P., Suksiriworapong, J., Chantasart, D., 2012. Physicochemical properties and skin permeation of Span 60/Tween 60 niosomes of ellagic acid. Int. J. Pharm. 423, 303–311.

Kaijser, G., Beijnen, J., Bult, A., Hogeboom, M., Underberg, W., 1991. A systematic study on the chemical stability of ifosfamide. J. Pharm. Biomed. Anal. 9, 1061–1067.

Kaul, S., Gulati, N., Verma, D., Mukherjee, S., Nagaich, U., 2018. Role of nanotechnology in cosmeceuticals: a review of recent advances. J. Pharm. 2018.

Kerbusch, T., de Kraker, J., Keizer, H.J., van Putten, J.W., Groen, H.J., Jansen, R.L., Schellens, J.H., Beijnen, J.H., 2001. Clinical pharmacokinetics and pharmacodynamics of ifosfamide and its metabolites. Clin. Pharmacokinet. 40, 41–62.

Khoee, S., Yaghoobian, M., 2017. Niosomes: A novel approach in modern drug delivery systems. Elsevier, In Nanostructures for drug delivery, pp. 207–237.

Kopec, S.E., Irwin, R.S., DeBellis, R.J., Bohlke, M.B., Maher, T.J., 2008. The effects of Tween-80 on the integrity of solutions of capsaicin: useful information for performing tussigenic challenges. Cough 4, 1–7.

Laraib, U., Sargazi, S., Rahdar, A., Khatami, M., Pandey, S., 2022. Nanotechnology-based approaches for effective detection of tumor markers: A comprehensive state-of-the-art review. Int. J. Biol. Macromol. 195, 356–383.

Liu, J., Qiu, Z., Wang, S., Zhou, L., Zhang, S., 2010. A modified double-emulsion method for the preparation of daunorubicin-loaded polymeric nanoparticle with enhanced in vitro anti-tumor activity. Biomed. Mater. 5, 065002.

Luqmani, Y., 2005. Mechanisms of drug resistance in cancer chemotherapy. Med. Princ. Pract. 14, 35–48.

Masotti, A., 2013. Niosomes as candidate bioconjugates for imaging and pH-sensitive drug delivery nanocarriers for rare pediatric tumors. J. Drug Delivery Sci. Technol. 23, 22–24.

Moghassemi, S., Hadjizadeh, A., 2014. Nano-niosomes as nanoscale drug delivery systems: an illustrated review. J. Control. Release 185, 22–36.

Mohamad Saimi, N.I., Salim, N., Ahmad, N., Abdulmalek, E., Abdul Rahman, M.B., 2021. Aerosolized niosome formulation containing gemcitabine and cisplatin for lung cancer treatment: Optimization, characterization and in vitro evaluation. Pharmaceutics 13, 59.

Mousa, A.M.; Allemailem, K.S.; Alhumaydhi, F.A.; Alrumaihi, F.; Almatroudi, A.; Aljasir, M.; Alwashmi, A.S.; Al Rugaie, O.; Soliman, K.E.; Aljohani, A.S. Cytoprotective Antioxidant, Anti-Inflammatory, and Antifibrotic Impact of Celery Seed Oil and Manuka Honey Against Cyclophosphamide-Induced Cystitis in Rabbits. Evidence-Based Complementary and Alternative Medicine 2022 (2022).

Nakata, H., Miyazaki, T., Iwasaki, T., Nakamura, A., Kidani, T., Sakayama, K., Masumoto, J., Miura, H., 2015. Development of tumor-specific caffeine-potentiated chemotherapy using a novel drug delivery system with Span 80 nano-vesicles. Oncol. Rep. 33, 1593–1598.

Nasr, M., Mansour, S., Mortada, N.D., Elshamy, A., 2008. Vesicular aceclofenac systems: a comparative study between liposomes and niosomes. J. Microencapsul. 25, 499–512.

Nasseri, B., 2005. Effect of cholesterol and temperature on the elastic properties of niosomal membranes. Int. J. Pharm. 300, 95–101.

Nikolaou, M., Pavlopoulou, A., Georgakilas, A.G., Kyrodimos, E., 2018. The challenge of drug resistance in cancer treatment: a current overview. Clin. Exp. Metastasis 35, 309–318.

Ohkawa, H., Ohishi, N., Yagi, K., 1979. Assay for lipid peroxides in animal tissues by thiobarbituric acid reaction. Anal. Biochem. 95, 351–358.

Özdemir, S., Kucukler, S., Çomaklı, S., Kandemir, F.M., 2022. The protective effect of Morin against ifosfamide-induced acute liver injury in rats associated with the inhibition of DNA damage and apoptosis. Drug Chem. Toxicol. 45, 1308–1317.

Pandit, A.A., Dash, A.K., 2011. Surface-modified solid lipid nanoparticulate formulation for ifosfamide: development and characterization. Nanomedicine 6, 1397–1412.

Rajera, R., Nagpal, K., Singh, S.K., Mishra, D.N., 2011. Niosomes: a controlled and novel drug delivery system. Biol. Pharm. Bull. 34, 945–953.

Roostaee, M., Sheikhshoaie, I., 2022. Fabrication of a sensitive sensor for determination of xanthine in the presence of uric acid and ascorbic acid by modifying a carbon paste sensor with Fe3O4@ Au core–shell and an ionic liquid. J. Food Meas. Charact. 16, 731–739.

Roostaee, M., Sheikhshoaei, I., Karimi-Maleh, H., 2022. Fe 3 O 4@ Au-rGO nanocomposite/ionic liquid modified sensor for ultrasensitive and selective sensing of doxorubicin. Top. Catal., 1–10.

Roostaee, M., Beitollahi, H., Sheikhshoaie, I., 2022. Simultaneous determination of dopamine and uric acid in real samples using a voltammetric nanosensor based on Co-MOF, graphene oxide, and 1-methyl-3-butylimidazolium bromide. Micromachines 13, 1834.

Safaei, M., Foroughi, M.M., Ebrahimpoor, N., Jahani, S., Omidi, A., Khatami, M., 2019. A review on metal-organic frameworks: Synthesis and applications. TrAC Trends Anal. Chem. 118, 401–425.

Salarpour, S., Barani, M., Pardakhty, A., Khatami, M., Chauhan, N.P.S., 2022. The application of exosomes and exosome-nanoparticle in treating brain disorders. J. Mol. Liq., 118549

Salvi, V.R., Pawar, P., 2019. Nanostructured lipid carriers (NLC) system: A novel drug targeting carrier. J. Drug Delivery Sci. Technol. 51, 255–267.

Saravani, R., Sargazi, S., Saravani, R., Rabbani, M., Rahdar, A., Taboada, P., 2020. Newly crocin-coated magnetite nanoparticles induce apoptosis and decrease VEGF expression in breast carcinoma cells. J. Drug Delivery Sci. Technol. 60, 101987.

Sargazi, S., Kooshkaki, O., Reza, J.Z., Saravani, R., Jaliani, H.Z., Mirinejad, S., Meshkini, F., 2019. Mild antagonistic effect of Valproic acid in combination with AZD2461 in MCF-7 breast cancer cells. Med. J. Islam Repub. Iran 33, 29.

Schwartzberg, L.S., Navari, R.M., 2018. Safety of polysorbate 80 in the oncology setting. Adv. Ther. 35, 754–767.

Sharma, V., Anandhakumar, S., Sasidharan, M., 2015. Self-degrading niosomes for encapsulation of hydrophilic and hydrophobic drugs: an efficient carrier for cancer multi-drug delivery. Mater. Sci. Eng. C 56, 393–400.

Sommer, B.r.; Dingersen, T.; Gamroth, C.; Schneider, S.E.; Rubert, S.; Krüger, J.; Dietz, K.-J. CELLmicrocosmos 2.2 MembraneEditor: a modular interactive shape-based software approach to solve heterogeneous membrane packing problems. Journal of chemical information and modeling 51 (2011) 1165-1182.

Sousa da Silva, A.W., Vranken, W.F., 2012. ACPYPE-Antechamber python parser interface. BMC. Res. Notes 5, 1–8.

Springate, J.E., Van Liew, J.B., 1995. Nephrotoxicity of ifosfamide in rats. J. Appl. Toxicol. 15, 399–402.

Suri, S.S., Fenniri, H., Singh, B., 2007. Nanotechnology-based drug delivery systems. J. Occup. Med. Toxicol. 2, 1–6.

Tavano, L., Muzzalupo, R., Mauro, L., Pellegrino, M., Andò, S., Picci, N., 2013. Transferrin-conjugated pluronic niosomes as a new drug delivery system for anticancer therapy. Langmuir 29, 12638–12646.

Twentyman, P.R., Luscombe, M., 1987. A study of some variables in a tetrazolium dye (MTT) based assay for cell growth and chemosensitivity. Br. J. Cancer 56, 279–285.

Ujhelyi, Z., Kalantari, A., Vecsernyés, M., Róka, E., Fenyvesi, F., Póka, R., Kozma, B., Bácskay, I., 2015. The enhanced inhibitory effect of different antitumor agents in self-microemulsifying drug delivery systems on human cervical cancer HeLa cells. Molecules 20, 13226–13239.

Vakiti, A.; Pilla, R.; Alhaj Moustafa, M.; Joseph, J.J.; Shenoy, A.G. Ifosfamide-induced metabolic encephalopathy in 2 patients with cutaneous T-cell lymphoma successfully treated with methylene blue. Journal of Investigative Medicine High Impact Case Reports 6 (2018) 2324709618786769.

Vanquelef, E., Simon, S., Marquant, G., Garcia, E., Klimerak, G., Delepine, J.C., Cieplak, P., Dupradeau, F.-Y., 2011. RED Server: a

web service for deriving RESP and ESP charges and building force field libraries for new molecules and molecular fragments. Nucleic Acids Res. 39, W511–W517.

Velmurugan, R., Nair, K.G., 2018. Toxicity evaluation of ifosfamide nanostructured lipid carriers designed for oral delivery in Wistar albino rats. Drug Invention Today 10.

Velmurugan, R., Selvamuthukumar, S., 2014. In vivo antitumor activity of a novel orally bioavailable ifosfamide nanostructured lipid carrier against Dalton's ascitic lymphoma. J. Pharm. Innov. 9, 203–211.

Velmurugan, R., Selvamuthukumar, S., 2016. Development and optimization of ifosfamide nanostructured lipid carriers for oral delivery using response surface methodology. Appl. Nanosci. 6, 159–173.

Verdeguer, A., Castel, V., Esquembre, C., Ferris, J., Fernandez, J.M., Ruiz, J.G., 1989. Fatal encephalopathy with ifosfamide/mesna. Pediatr. Hematol. Oncol. 6, 383–385.

Wang, S.-Q., Zhang, Q., Sun, C., Liu, G.-Y., 2018. Ifosfamide-loaded lipid-core-nanocapsules to increase the anticancer efficacy in MG63 osteosarcoma cells. Saudi J. Biol. Sci. 25, 1140–1145.

Zahreddine, H., Borden, K.L., 2013. Mechanisms and insights into drug resistance in cancer. Front. Pharmacol. 4, 28.

Zhao, L., Yuan, W., Li, J., Yang, L., Su, Y., Peng, J., Chen, R., Tham, H.P., Chen, H., Lim, W.Q., 2018. Independent of EPR effect: A smart delivery nanosystem for tracking and treatment of nonvascularized intra-abdominal metastases. Adv. Funct. Mater. 28, 1806162.